IEEE Access
Multidisciplinary | Rapid Review | Open Access Journal

Received August 7, 2019, accepted September 6, 2019, date of publication September 23, 2019, date of current version October 4, 2019.

Digital Object Identifier 10.1109/ACCESS.2019.2942941

Three Dimensional Image-Based Radar Cross Section Extrapolation via Planar Projective Transforms

LING PU, (Student Member, IEEE), XIAOLING ZHANG, JUN SHI, SHUNJUN WEI, (Member, IEEE), LIANG LI, AND XINXIN TANG, (Student Member, IEEE)

University of Electronic Science and Technology of China, Chengdu, China

Corresponding author: Ling Pu (puling@std.uestc.edu.cn)

This work was supported in part by the National Key Research and Development Program of China under Grant 2017YFB0502700, and in part by the National Natural Science Foundation of China under Grant 61571099, Grant 61501098, and Grant 61671113.

ABSTRACT Conventional radar cross section (RCS) measurements require far-field or compact-antenna-test-range (CATR) conditions, which have strict restrictions and high implementation costs. By contrast, RCS extrapolation methods in the near zone are more convenient and practical, which become the research emphasis in recent years. This paper presents a novel RCS extrapolation method based on the combination of near-field 3D synthetic aperture radar (SAR) technique and planar projective transforms (PPT) algorithm. Firstly, to extract the target's reflectivity distribution, we apply near-field 3D SAR imaging and obtain 3D near-field RCS (NFRCS) images. Secondly, to meet the requirement of RCS measurements, we derive a novel correction factor used to precisely expand 3D NFRCS images. Finally, we extrapolate the plane-wave responses in the azimuth-vertical dimensions, which presents as planar patterns. The proposed method utilizes the complete 3D image-based information to overcome the inherent constraints of classical RCS extrapolation methods on application scenarios, which has the advantages of broad applicability and high flexibility. The detailed derivation and implementation of this method are described in this paper. The simulation and experiment results verify that the proposed method can provide the equivalent CATR result within $\pm 11^\circ$ azimuth and elevation angles, and it is applicable to precisely measuring the point, surface, and complex scatterers.

INDEX TERMS Radar cross section, synthetic aperture radar, near-field 3D imaging, far-field extrapolation, planar projective transforms.

I. INTRODUCTION

Radar cross section (RCS) is a critical parameter that represents the ability of targets to reflect and scatter electromagnetic (EM) waves. It is correlated with the geometrical parameters and physical parameters of targets, such as shape, size, and material. Meanwhile, it is also correlated with the EM propagation parameters, such as frequency, polarization, and azimuth. RCS measurements are significant in the fields of EM scattering researches, radar design, and target identification [1]–[3].

Generally, the difficulties of RCS measurements are to meet the requirement of plane-wave illumination [1] and isolate targets from environments. As for conventional outdoor RCS measurements, the range between the measured target and radar system should be far enough. However, this approach is easily disturbed by outdoor environments. Many interference sources, including ground reflection [4], clutter, and noise, affect the accuracy of conventional outdoor RCS measurements. As for conventional indoor RCS measurements, microwave anechoic chambers are usually applied to isolate environments. However, the chambers may not meet the far-field criterion [14], which commonly needs compact-antenna-test-range (CATR) [5], [6] conditions. Besides, it is hard to provide CATR conditions for large objects (such as full-scale aircraft) and some new-type radar (such as array radar [7], [8] and SAR [9]–[11]). As a result, conventional RCS measurements have many strict restrictions on environments, measured objects, and equipment.

The associate editor coordinating the review of this manuscript and approving it for publication was Yang Li.

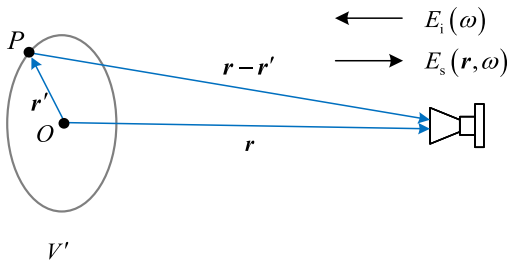

FIGURE 1. Relationship between a scatterer and a single sensor.

When the far-field criterion and plane-wave illumination can not be satisfied, RCS extrapolation, or called near-field to far-field transformation (NFFFT), can be applied to correct radiation distortion in the near zone. At present, the widely used RCS extrapolation techniques, including the 1D high resolution range profile (HRRP) [12], [13] extrapolation and the 2D inverse synthetic aperture radar (ISAR) [14]–[17] extrapolation, can correct the range dimension or the azimuth dimension. However, the information about the elevation dimension (third dimension) is missing. When the test range becomes shorter, the unsolved 3D information becomes the residual phase [18], [19], which may affect the measurement accuracy. For these reasons, traditional 1D and 2D techniques commonly require the elevation dimension must meet the far-field criterion. As for electrically large objects, it is still hard to meet this requirement.

With the development of radar techniques, near-field 3D SAR [20]–[24], which combines the wide-band radar signal processing and antenna-array processing, is becoming one of the hotspots. This new technique can resolve the three radiation directions, including the time (range), azimuth, and elevation directions, and can present the target's reflectivity as high-resolution 3D images. Compared with traditional 1D and 2D techniques, near-field 3D SAR has a distinct advantage of accuracy, which tends to be helpful for RCS measurements.

Therefore, this paper studies the 3D image-based RCS extrapolation method. The rest of this paper is organized as follows. In section 2, the basic radar scattering models are given. In section 3, the proposed method is derived in detail. The simulation verification is shown in section 4. The experiment verification is shown in section 5. Finally, the conclusion of this paper is presented in section 6.

II. BASIC MODELS

A. RCS MEASUREMENT MODEL

At first, a fundamental relationship between a scatterer and a single sensor is shown in Fig. 1, where O denotes the scattering center, $\boldsymbol{r}$ denotes the range vector from the scattering center to the sensor, $\boldsymbol{r}'$ denotes the range vector from the scattering center to the scatterer's boundary, ω denotes the angular frequency, $E_i(\omega)$ denotes the incident field at the source, and $E_s(\boldsymbol{r}, \omega)$ denotes the scattered field.

Considering the round-trip propagation, the scattered field based on the physical optical approximation [23], [24] can be expressed as

$$E_s(\boldsymbol{r}, \omega) \approx \int_{V'} j\omega\delta(\boldsymbol{r}')[G(\boldsymbol{r}, \boldsymbol{r}', \omega)]^2 d^3\boldsymbol{r}' \tag{1}$$

$$G(\boldsymbol{r}, \boldsymbol{r}', \omega) = \frac{e^{-j\omega|\boldsymbol{r}-\boldsymbol{r}'|/c}}{4\pi|\boldsymbol{r}-\boldsymbol{r}'|} \tag{2}$$

where V' denotes the volume of the measured target, and c denotes light speed. $\delta(\boldsymbol{r}')$ denotes the reflectivity distribution function [24], which describes the strength of the induced EM field. $G(\boldsymbol{r}, \boldsymbol{r}', \omega)$ denotes the Green's function [23], which is critical for explaining the propagation effects from scattering sources into the specific range. Here the Green's function is squared to describe the round-trip propagation.

When $|\boldsymbol{r}| \gg |\boldsymbol{r}'|$, we assume that the Green's function is planar and uniform. In this case, we can calculate the far-field RCS by using the following formula:

$$\sigma_{far} = (4\pi|\boldsymbol{r}|^2)^2 \frac{|E_s(\boldsymbol{r}, \omega)|^2}{|E_i(\omega)|^2} \tag{3}$$

Based on (3), RCS measurement techniques can evaluate the ability of a target to reflect and scatter EM waves. In practical, conventional RCS measurements should meet the far-field criterion:

$$|\boldsymbol{r}| > \frac{2D^2}{\lambda} \tag{4}$$

where λ denotes the wavelength, and D denotes the larger value between the antenna aperture and the target's diameter. When the wavelength becomes narrower and the measured target becomes larger, it is hard to meet (4) directly. For example, the far-field range for a large target with 20 m diameter illuminated with 10 GHz ($\lambda = 0.03$ m) radiation should extend out as far as 25 km.

Compared with far-field measurements, near-field RCS (NFRCS) measurements are more convenient. However, when a measured target is in the near zone (Fresnel zone), the Green's function becomes spheroidal, which causes the dramatic change of scattered fields. As a result, the near-field patterns are different from the far-field patterns significantly.

In order to solve this problem, the conventional way is to adopt some equipment or physical means, such as the plane-wave generators combined with CATR conditions. However, the implementation costs are commonly pretty high. Besides, the equivalent far zone, size of measured targets, available frequencies, and applicable radar mode are limited strictly.

With the deepening of EM scattering researches, radar techniques, and radar signal processing, RCS extrapolation methods, which have few restrictions and high flexibility, gradually become the research emphasis in recent years.

B. NEAR-FIELD RCS EXTRACTION VIA 3D SAR IMAGING

Near-field 3D SAR technique, which develops rapidly in the fields of security check and intelligent automotive radar,

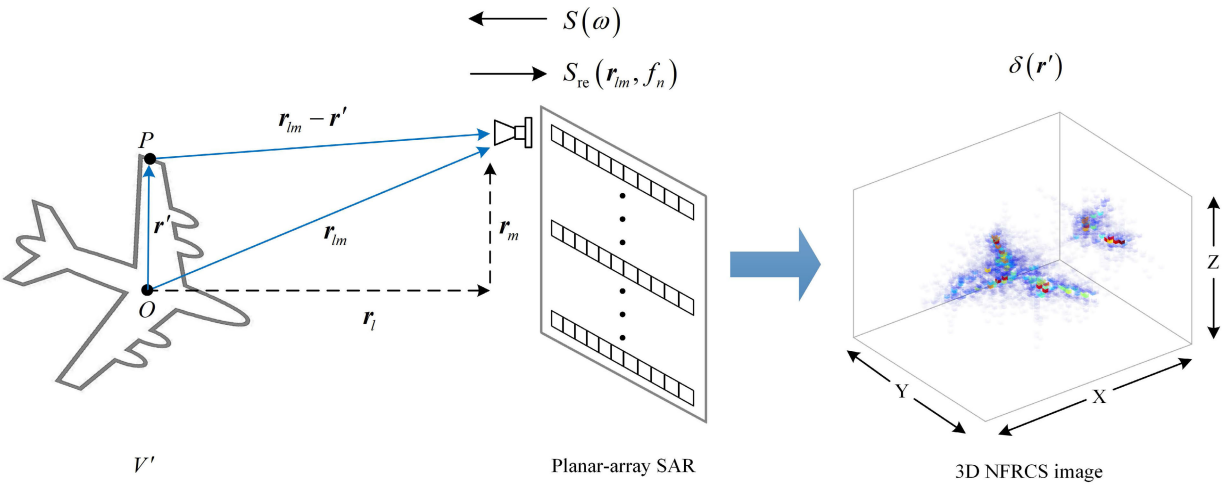

FIGURE 2. Near-field 3D SAR imaging model.

achieves the 3D imaging for the measured target in the short range. Fig. 2 shows a near-field 3D SAR imaging model. The measured target is placed in a fixed position. Then, the planar-array SAR is set up in the near zone and illuminates the measured target coherently.

Given the step-frequency [25] signal waveform $S(f_n)$, $n = 1, 2, ..., N$, where n denotes the frequency point and $f_n = f_0 + (n - N/2)\triangle f$. Given the planar-array SAR expressed by a group of sensors $\boldsymbol{r}_{lm} = \boldsymbol{r}_l + \boldsymbol{r}_m$, $l = 1, 2, ..., L$, $m = 1, 2, ..., M$, where l is the azimuth sampling point and m is elevation sampling point. The received echoes can be expressed in the following:

$$E_{re}(\boldsymbol{r}_{lm}, f_n) = PS(f_n)E_s(\boldsymbol{r}_{lm}, f_n) \tag{5}$$

where P denotes the remaining parameters in the radar equation [26].

To obtain well-focused 3D images, it is necessary to fully compensate the spherical-wave effects coming from the time (range), azimuth, and elevation dimensions. The widely adopted spherical-wave compensation operators [27], [28] are derived by calculating Green's functions backward, whose expression is

$$\begin{aligned} G^{-1}(\boldsymbol{r}_{lm}, \boldsymbol{r}', f_n) &= [\frac{e^{j4\pi(f_n - f_0)R_0/c}}{f_n}] \cdot [\frac{(4\pi R_0)^2 e^{j4\pi f_0 R_0/c}}{j^2 A}] \\ &= \Phi_1(f_n) \cdot \Phi_2(\boldsymbol{r}_{lm}) \end{aligned} \tag{6}$$

where A denotes the antenna patterns, and $R_0 = |\boldsymbol{r}_{lm} - \boldsymbol{r}'|$ denotes the near-field range. The compensation operators $G^{-1}(\boldsymbol{r}_{lm}, \boldsymbol{r}', f_n)$ can be divided into the two subfunctions $\Phi_1(f_n)$ and $\Phi_2(\boldsymbol{r}_{lm})$. $\Phi_1(f_n)$ is used to resolve the time dimension via the frequency scanning. $\Phi_2(\boldsymbol{r}_{lm})$ is used to resolve the remaining dimensions by matching the azimuth and elevation variables.

In terms of SAR focusing, 3D back-projection (BP) [27] technique is especially useful for compensating the spherical-wave effects in near-field conditions. Thus we apply 3D BP technique to compensate the terms in (6), which can be expressed as

$$\begin{aligned} \widehat{\delta}(\boldsymbol{r}') &= \sum_{m=1}^{M}\sum_{l=1}^{L}[\sum_{n=1}^{N} E_{re}(\boldsymbol{r}_{lm}, f_n)\Phi_1(f_n)]\Phi_2(\boldsymbol{r}_{lm}) \\ &= \sum_{m=1}^{M}\sum_{l=1}^{L}\delta_1(f_0)\Phi_2(\boldsymbol{r}_{lm}) \\ &= \delta_1(f_0) * \delta_2(R_0) \end{aligned} \tag{7}$$

where $*$ denotes convolution, $\delta_1(f_0)$ denotes the system's Dirac delta function [30] at f_0, $\delta_2(R_0)$ denotes the system's point spread function (PSF) [26] at R_0, and $\widehat{\delta}(\boldsymbol{r}')$ denotes the complex-valued reflectivity.

After data processing, we acquire a 3D NFRCS image, which visually describes the target's reflectivity distribution. Besides, this technique ensures the easy implementation by using the single-input-single-output (SISO) array via the spatial motion of a single sensor, or the multiple-input-multiple-output (MIMO) array via the spatial distribution of multiple sensors. Thus the application of near-field 3D SAR imaging tends to be helpful for EM scattering researches and RCS measurements.

III. 3D IMAGE-BASED RCS EXTRAPOLATION VIA PLANAR PROJECTIVE TRANSFORMS

A. DERIVATION OF PLANAR PROJECTIVE TRANSFORMS

According to Huygens-Fresnel's principle [31], the patterns in the near zone (Fresnel zone) can be considered as the sources of secondary radiation and expanded into the far zone (Fraunhofer zone), which is the basis of RCS extrapolation and has been verified in 1D and 2D RCS measurements.

Given a correction factor $\widetilde{\boldsymbol{r}}$ meeting the criterion in (4), we consider the near-field reflectivity $\delta(\boldsymbol{r}')$ as Huygens

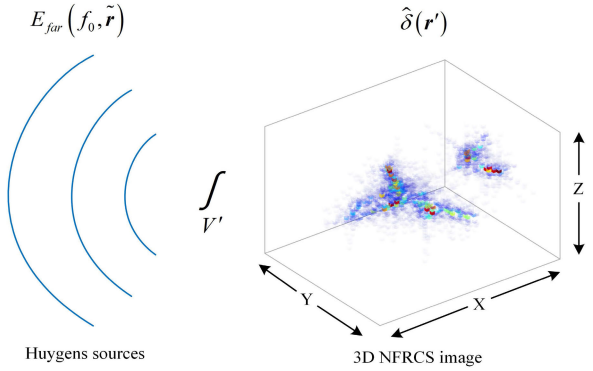

FIGURE 3. 3D image-based RCS extrapolation.

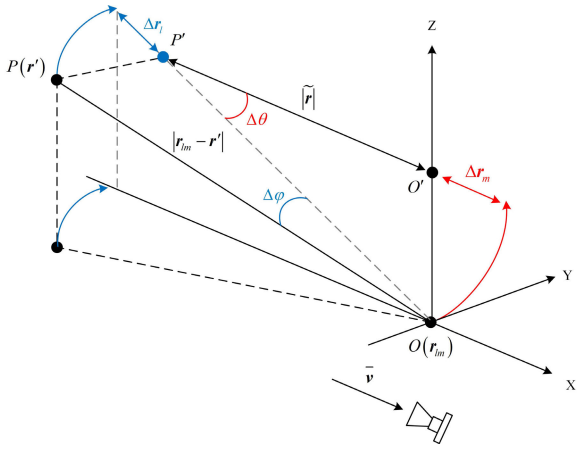

FIGURE 4. 3D correction factor in the proposed algorithm.

sources and give a basic extrapolation model by using

$$E_{far}(f_0,\tilde{\boldsymbol{r}})=\int_{V'}\delta(\boldsymbol{r}')\frac{e^{-j4\pi f_0|\tilde{\boldsymbol{r}}|/c}}{(4\pi|\tilde{\boldsymbol{r}}|)^2}d^3\boldsymbol{r}' \tag{8}$$

where $E_{far}(f_0,\tilde{\boldsymbol{r}})$ is the expected far-field patterns.

From (8), the near-field to far-field transformation relationship is constructed via the integral calculation of the complete 3D information of scenarios. However, in practical, traditional 1D and 2D RCS measurements lack the complete 3D information. For this reason, classical RCS extrapolation methods, such as the method by using the fast Fourier transforms (FFT) [10], the method by using the Hankel transforms (HT) [29], and so on, have to set the inherent constraints, including that the target's elevation dimension must meet far-field conditions and the target's azimuth dimension should be highly consistent with the scattering center [10]. As for electrically large objects, it is still hard to meet these constraints. Besides, classical RCS extrapolation methods adopt the dimensional-reduction approximations for (8), which may further restrict application scenarios and measurement accuracy.

To overcome the above problems commonly appearing in traditional 1D and 2D RCS measurements, we note that the near-field 3D SAR imaging model described in section 2 can precisely acquire the 3D information of scenarios. By using (7), we have 3D NFRCS images without the dimensional-reduction approximations. Therefore, considering 3D NFRCS images as Huygens sources can derive the more accurate extrapolation model in principle.

Substituting (7) into (8), we have

$$\begin{aligned}E_{far}(f_0,\tilde{\boldsymbol{r}})&=\int_{V'}[\delta_1(f_0)*\delta_2(R_0)]\frac{e^{-j4\pi f_0|\tilde{\boldsymbol{r}}|/c}}{(4\pi|\tilde{\boldsymbol{r}}|)^2}d^3\boldsymbol{r}'\\&=\delta_1(f_0)\int_{V'}\sum_{m=1}^{M}\sum_{l=1}^{L}\Phi_2(\boldsymbol{r}_{lm})\frac{e^{-j4\pi f_0|\tilde{\boldsymbol{r}}|/c}}{|\tilde{\boldsymbol{r}}|^2}d^3\boldsymbol{r}'\end{aligned} \tag{9}$$

where $\delta_1(f_0)$ is considered to be constant during this processing.

From (9), we see that the expansion of $\delta_2(R_0)$ is variable with the term $\Phi_2(\boldsymbol{r}_{lm})$ in the 3D image domain. In this case, we should consider whether the model shown in (9) meets the uniformity compared with the ideal plane-wave model. Here, we consider $\delta_2(R_0)$ as a scattering center at R_0. As for a point target, this expansion is appropriate. As for a volume target with multiple scattering centers, however, this expansion commonly does not meet the uniformity. The reason is that the correction factor $\tilde{\boldsymbol{r}}$ only meeting far-field conditions is not clear enough to solve the azimuth-elevation variation in the 3D image domain. Without the exact correction, this variation eventually reflects on the extrapolation result, which may cause some differences between our model and the ideal plane-wave model.

Therefore, we should further refine the correction factor $\tilde{\boldsymbol{r}}$ in (9) in order to construct the exact projective relation between the 3D image domain and the specific scattered field.

Given the resulting 3D NFRCS image in Cartesian coordinates $[x, y, z]$, we firstly import a specific direction vector as

$$\bar{\boldsymbol{v}}=[\cos\varphi\sin\theta,\sin\varphi\sin\theta,\cos\theta] \tag{10}$$

where φ is the azimuth angle, and θ is the elevation angle.

Then, we have a new range value as the projection along the specific direction by using

$$|\tilde{\boldsymbol{r}}|=\bar{\boldsymbol{v}}\cdot(\boldsymbol{r}_{lm}-\boldsymbol{r}') \tag{11}$$

Let $\boldsymbol{r}_{lm}=\boldsymbol{r}_l+\boldsymbol{r}_m$, where $\boldsymbol{r}_l$ and $\boldsymbol{r}_m$ denote the current sensor. And then, we expand (11) as

$$\begin{aligned}|\tilde{\boldsymbol{r}}|&=\bar{\boldsymbol{v}}\cdot(\boldsymbol{r}_l+\boldsymbol{r}_m-\boldsymbol{r}')\\&=|\tilde{\boldsymbol{r}}_l(\textstyle\bigtriangleup\varphi)|+|\tilde{\boldsymbol{r}}_m(\bigtriangleup\theta)|-\bar{\boldsymbol{v}}\cdot\boldsymbol{r}'\end{aligned} \tag{12}$$

Fig. 4 visually shows the new correction factor. As for a 3D image unit in $P(\boldsymbol{r}')$ and a sensor in $O(\boldsymbol{r}_{lm})$, the raw scattered field based on $(\boldsymbol{r}_{lm}-\boldsymbol{r}')$ is distorted. The correction factor $|\tilde{\boldsymbol{r}}|$ is derived by using a azimuth-directional projection $|\boldsymbol{r}_l|\rightarrow|\tilde{\boldsymbol{r}}_l(\bigtriangleup\varphi)|$ and another elevation-directional projection $|\boldsymbol{r}_m|\rightarrow|\tilde{\boldsymbol{r}}_l(\bigtriangleup\theta)|$. After that, weighting the remaining factor $(\bar{\boldsymbol{v}}\cdot\boldsymbol{r}')$ into a 3D NFRCS image can extrapolate the plane-wave response in the direction of (φ,θ).

Therefore, we consider substituting (12) into (9) and forming the projective relation between a 3D NFRCS image and the expected far-field patterns, and finally solving the integral transforms. Here we called the above process as the planar projective transforms (PPT) in this paper.

B. ALGORITHM IMPLEMENTATION OF PLANAR PROJECTIVE TRANSFORMS

We implement the PPT algorithm for the 3D image-based RCS extrapolation, whose steps are as follows.

Firstly, let the sensor at $\boldsymbol{r}_{lm}$ and 3D image-based reflectivity distribution $\widehat{\delta}(\boldsymbol{r}')$ be the input.

Then, we expand the reflectivity distribution by using the following operation:

$$K = \sum_{m=1}^{M} \sum_{l=1}^{L} e^{-j4\pi f_0(|\widetilde{\boldsymbol{r}}_l(\triangle\varphi)|+|\widetilde{\boldsymbol{r}}_m(\triangle\theta)|)/c} \tag{13}$$

Through traversing the 3D image domain, we use the integral transforms in the following:

$$\widehat{E}_{far}(f_0, \varphi, \theta) = K \int_{V'} w(\boldsymbol{r}')\widehat{\delta}(\boldsymbol{r}') \frac{e^{j4\pi f_0|\bar{\boldsymbol{v}}\cdot\boldsymbol{r}'|/c}}{|\bar{\boldsymbol{v}}\cdot\boldsymbol{r}'|^2} d^3\boldsymbol{r}' \tag{14}$$

where $w(\boldsymbol{r}')$ is a window function to truncate the region beyond the limit condition:

$$\begin{cases} |\triangle\varphi| \le \arctan(\dfrac{D_a}{2R_0}) \\ |\triangle\theta| \le \arctan(\dfrac{D_e}{2R_0}) \end{cases} \tag{15}$$

where D_a and D_e denote the apertures of planar-array SAR.

Finally, use a calibrator to normalize the remaining coefficients $\delta_1(f_0)$ in (9). The extrapolated RCS patterns at (f_0, φ, θ) is calibrated as

$$\widehat{\sigma}_{far}(f_0, \varphi, \theta) = |\frac{4\pi\widehat{E}_{far}(f_0, \varphi, \theta)}{\delta_1(f_0)}|^2 \tag{16}$$

By utilizing the complete 3D image-based information, the proposed method overcomes the inherent constraints of classical RCS extrapolation methods on application scenarios. For instance, there are no constraints on the target's elevation dimension in our method. Therefore, the proposed method can extrapolate the plane-wave responses in both the azimuth and vertical dimensions, which has the advantages of broad applicability and high flexibility.

IV. SIMULATION VERIFICATION

In order to verify the effectiveness of the proposed method, a series of simulations have been implemented.

A. POINT SCATTERER

In Fig. 5(a), a point scatterer with the normalized amplitude and phase is illuminated by using a planar-array SAR with 2×2 m^2 size ($\pm 12.5°$ azimuth and elevation angles), and the range between the illumination center and the point scatterer is 4.5 m. The transmitted signal is the SF signal with 10 GHz center frequency and 2 GHz bandwidth. Given $\lambda = 0.03$ m and $D = 2$ m, the far-field criterion according to (4) is about 267 m. Thus this model works in the Fresnel zone. By using 3D BP technique, we obtain a 3D scattering center and present it as an image, as shown in Fig. 5(b).

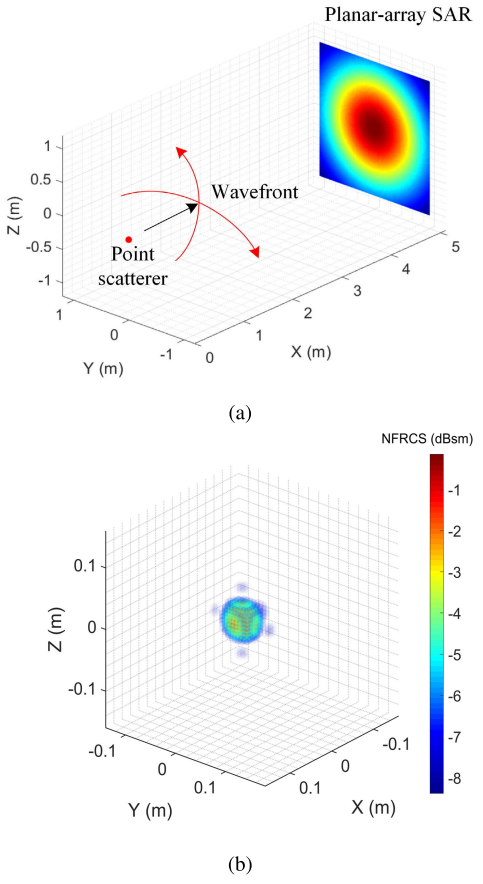

FIGURE 5. (a) A normalized point scatterer, illuminated by the planar-array SAR. (b) 3D NFRCS image of a point scatterer.

Considering this image as Huygens sources, the raw amplitude and phase patterns are shown in Fig. 6(a) and (b) respectively. Fig. 6(c) and (d) show the amplitude and phase variation at $\theta = 0°$. It can be observed from these results that the near-field patterns change drastically. According to the standard of CATR [6], the amplitude variation should be within ± 1 dB, and the phase variation should be within $\pm 5°$ in general. In the near-field patterns, there is a very narrow zone within $\pm 1°$ meets the CATR standard. In other words, this near-field 3D SAR model without correction requires that the variation of radiation angles is less than $\pm 1°$, which is still strict.

We firstly use the classical fast Fourier transforms (FFT) algorithm [10] to extrapolate far-field patterns from the 3D image. Fig. 7(a) and (b) show the extrapolated amplitude and phase patterns by using FFT. It can be observed that the radiation distortion is corrected in some degrees. Fig. 7(c) and (d) show the amplitude and phase variation via FFT. According to the CATR standard, the limit condition via FFT is within $\pm 6°$. The zone beyond $\pm 6°$ has a serious boundary effect and greater variation.

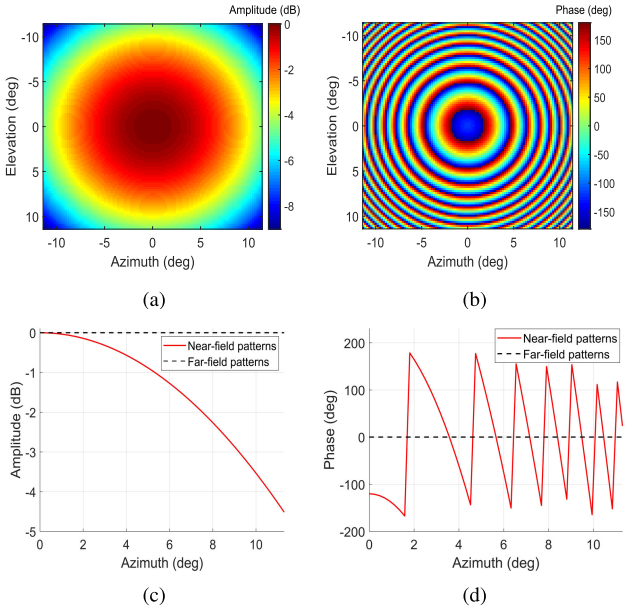

FIGURE 6. Raw near-field patterns. (a) Amplitude plane. (b) Phase plane. (c) Amplitude profile at $\theta = 0°$. (d) Phase profile at $\theta = 0°$.

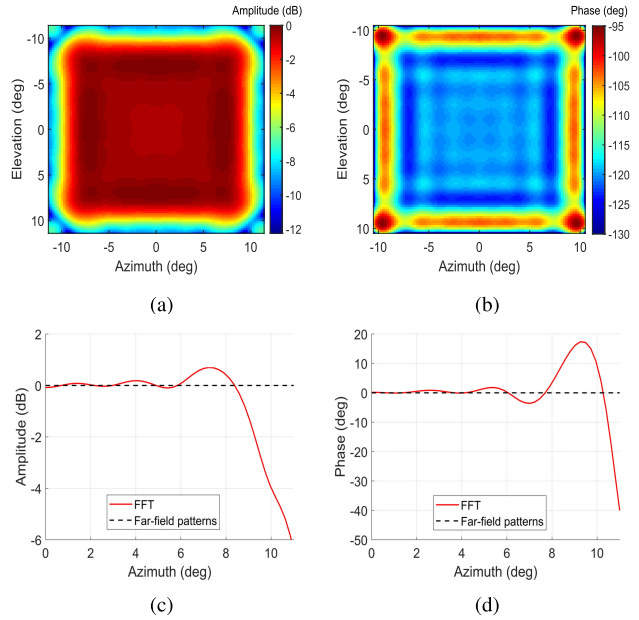

FIGURE 7. Extrapolated patterns via classical FFT. (a) Amplitude plane. (b) Phase plane. (c) Amplitude profile at $\theta = 0°$. (d) Phase profile at $\theta = 0°$.

Then, we use the classical Hankel transforms (HT) algorithm [29] to extrapolate far-field patterns. Fig. 8(a) and (b) show the extrapolated amplitude and phase patterns by using HT. Fig. 8(c) and (d) show the amplitude and phase variation via HT. According to the CATR standard, the limit condition via HT is within $\pm 9°$, which is slightly better than FFT.

And then, we use the proposed PPT algorithm to extrapolate far-field patterns. Fig. 9(a) and (b) show the extrapolated amplitude and phase patterns by using PPT.

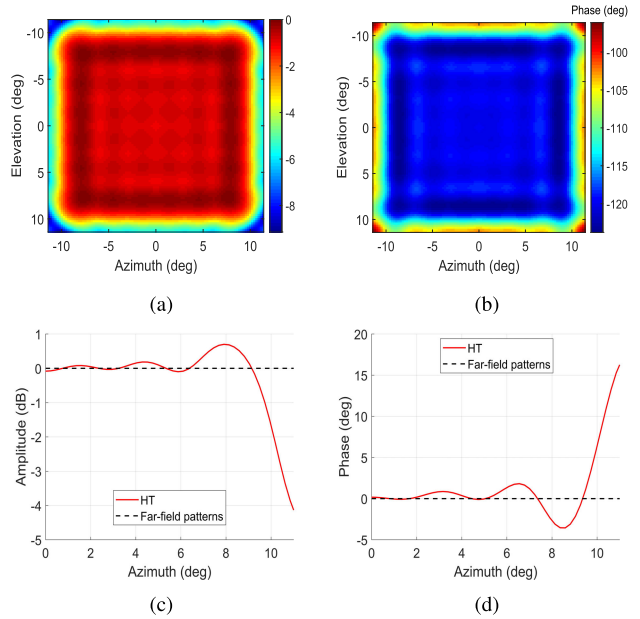

FIGURE 8. (a) Extrapolated patterns via classical HT. (a) Amplitude plane. (b) Phase plane. (c) Amplitude profile at $\theta = 0°$. (d) Phase profile at $\theta = 0°$.

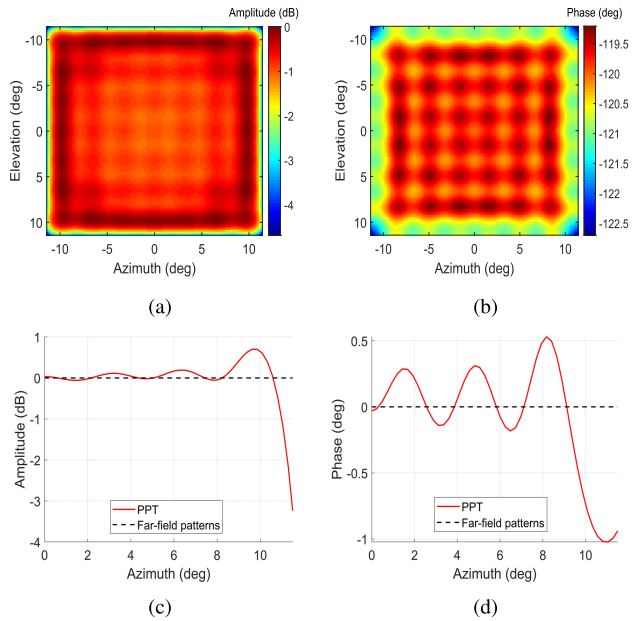

FIGURE 9. Extrapolated patterns via the proposed PPT algorithm. (a) Amplitude plane. (b) Phase plane. (c) Amplitude profile at $\theta = 0°$. (d) Phase profile at $\theta = 0°$.

Fig. 9(c) and (d) show the amplitude and phase variation via PPT. It can be observed that the radiation distortion is corrected precisely. According to the CATR standard, the limit condition via the proposed method is within $\pm 11°$.

By comparing the limit condition, the proposed method is more robust than the classical FFT and HT methods even if the azimuth and elevation angles become larger. It indicates that the proposed method can provide the equivalent CATR

TABLE 1. Performance comparison of different methods within ±5° azimuth degrees.

Methods	Amplitude deviation	Phase deviation
FFT	±0.19 dB	±1.5 deg
HT	±0.18 dB	±0.9 deg
PPT	±0.12 dB	±0.3 deg

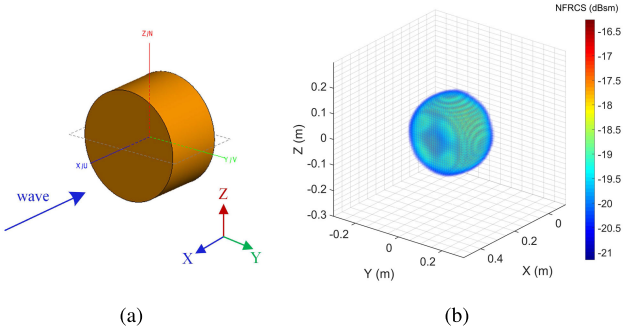

FIGURE 10. (a) Metal cylinder. (b) 3D NFRCS image of a metal cylinder.

result in a relatively large region, which is more effective for measuring electrically large targets.

Additionally, Table 1 shows the performance comparison of different methods within small azimuth angles (±5°). The amplitude correction of different methods is similar, and the proposed PPT method performs better in phase correction.

Therefore, as for the RCS extrapolation of a scattering center acquired by near-field 3D SAR imaging, the proposed method is superior to the classical FFT and HT methods.

B. CYLINDER SCATTERER

Cylinder scatterers have the typical RCS function and are widely researched in RCS measurements [14]. Based on EM numerical simulation, a metal cylinder (179 mm high and 300 mm wide), as shown in Fig. 10(a), is illuminated by using a VV polarized planar-array SAR with 2×2 m^2 size, and the range between the illumination center and the cylinder is 4.5 m. The transmitted signal is the SF signal with 11 GHz center frequency and 2 GHz bandwidth. By using 3D BP algorithm, we acquire the 3D NFRCS image of the metal cylinder, as shown in Fig. 10(b).

Considering this 3D NFRCS image as Huygens sources, the raw RCS patterns along the azimuth angle φ and elevation angle θ are shown in Fig. 11(a). For comparison, we use the physical optics (PO) [31] method to calculate the theoretical far-field RCS patterns, and the result is shown in Fig. 11(b). Then, we use the proposed PPT algorithm to extrapolate the far-field RCS patterns from the 3D NFRCS image, and the result is shown in Fig. 11 (c). Fig. 11 (d) shows the profile result when $\theta = 0°$.

It can be observed that the raw near-field patterns are different from the theoretical far-field patterns. Meanwhile, there is a high correlation between the PPT result and theoretical value. Within ±11° azimuth and elevation angles, the mean deviation between the near-field patterns and far-field patterns is 8.56 dB, and the mean deviation between the PPT result and far-field patterns is only 1.96 dB.

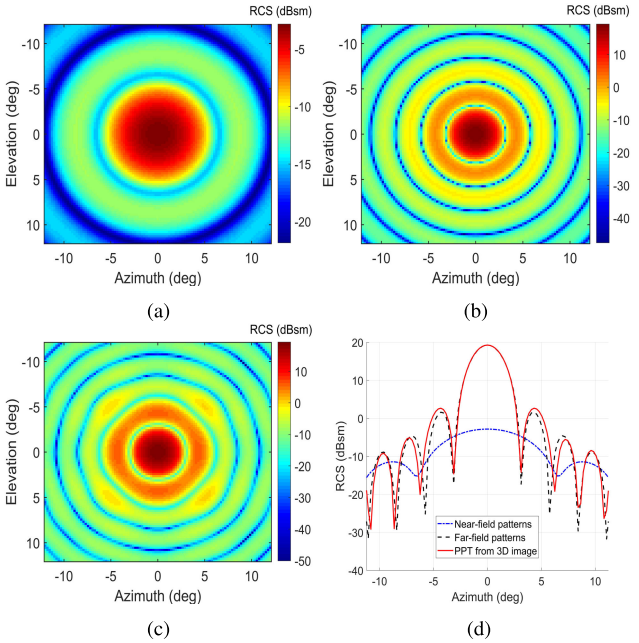

FIGURE 11. RCS patterns of a metal cylinder in the azimuth and elevation directions. (a) Near-field patterns. (b) Theoretical far-field patterns. (c) Extrapolated patterns via the proposed method. (d) Profile result at $\theta = 0°$.

From these results, we recover the multi-directional far-field patterns of a metal cylinder, which verifies the proposed method is applicable to precisely measuring surface scatterers.

C. COMPLEX SCATTERER

In the next stage, a complex metal aircraft model (about 1.3 m lengths, 1 m wide, and 0.3 m height), as shown in Fig. 12(a), is illuminated by using a VV polarized planar-array SAR with 2×2 m^2 size, and the range between the illumination center and the aircraft model is 4.5 m. The transmitted signal is the SF signal with 9 GHz center frequency and 2 GHz bandwidth.

Fig. 12(b) and (c) shows the 3D NFRCS image representing the forward scattering of this aircraft model. It can be detected from the image that this aircraft model has the relatively complex reflectivity distribution, including the multiple reflections of the air-inlet structures and the edge diffraction of the back.

Considering this 3D NFRCS image as Huygens sources, the raw RCS patterns derived from the 3D NFRCS image are shown in Fig. 13(a). For comparison, we use the PO method to calculate the theoretical far-field RCS patterns, as shown in Fig. 13(b). Then, we use the proposed PPT algorithm to extrapolate the far-field RCS patterns from the 3D NFRCS image, and the result is shown in Fig. 13 (c). Fig. 14 (a) shows the profile result when $\theta = 0°$. Fig. 14 (b) shows the profile result when $\varphi = 0°$.

It can be observed that there is some otherness between the near-field patterns and theoretical far-field patterns. Meanwhile, there is a high correlation between the PPT result and theoretical far-field patterns. Within ±11° azimuth and

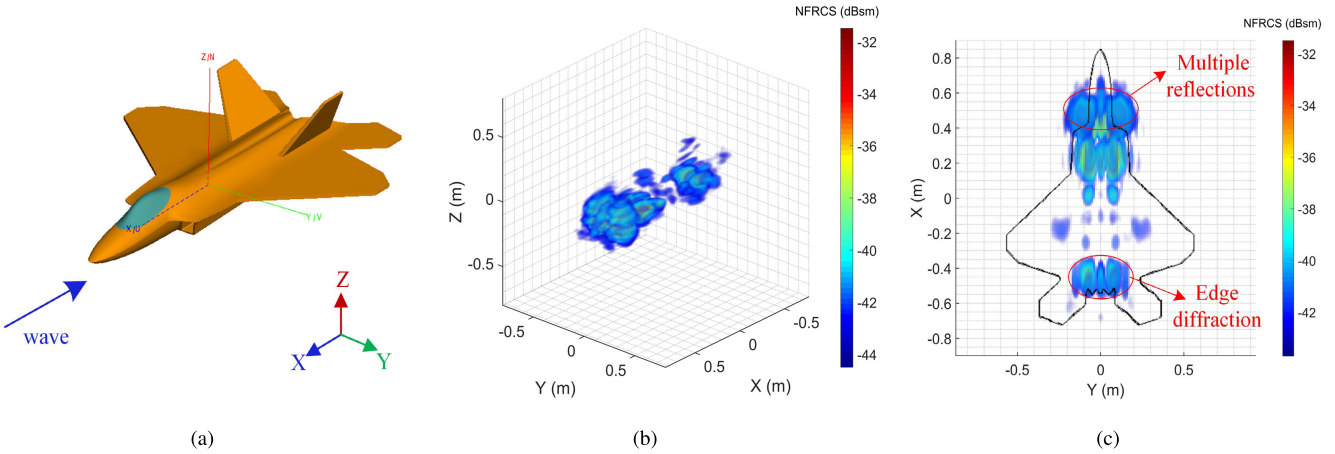

FIGURE 12. (a) Metal aircraft model. (b) and (c) show the 3D NFRCS image of a metal aircraft model.

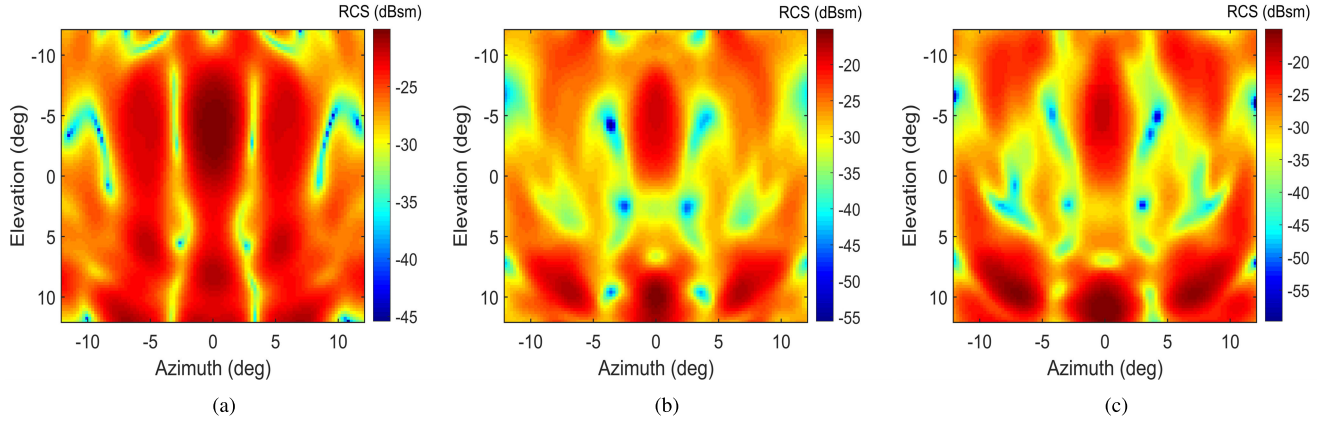

FIGURE 13. RCS patterns of a aircraft model in the azimuth and elevation directions. (a) Near-field patterns. (b) Theoretical far-field patterns. (c) Extrapolated patterns via the proposed method.

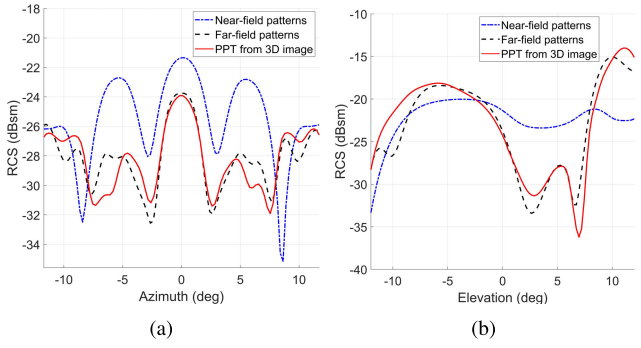

FIGURE 14. Profile results for a metal aircraft model. (a) $\theta = 0°$. (b) $\varphi = 0°$.

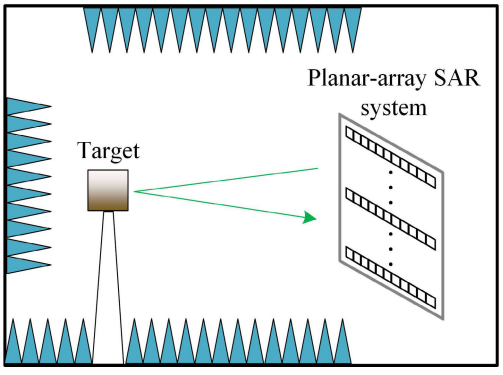

FIGURE 15. Experimental scene.

elevation angles, the mean deviation between the near-field patterns and far-field patterns is 4.31 dB, and the mean deviation between the PPT result and far-field patterns is only 1.67 dB.

From these results, we recover the multi-directional far-field patterns of an aircraft model, which verifies the proposed method is applicable to precisely measuring complex scatterers.

V. EXPERIMENTAL VERIFICATION

We have implemented some actual experiments to further test the effectiveness of the proposed method. The experimental scene is in a microwave anechoic chamber, as shown in Fig. 15. A planar-array SAR system with 1.5×1.5 m^2 size illuminates the target coherently, and the test range is about 4.8 m. The transmitted signal is the SF signal generated by the N5244A PNA-X microwave network analyzer with 10 GHz

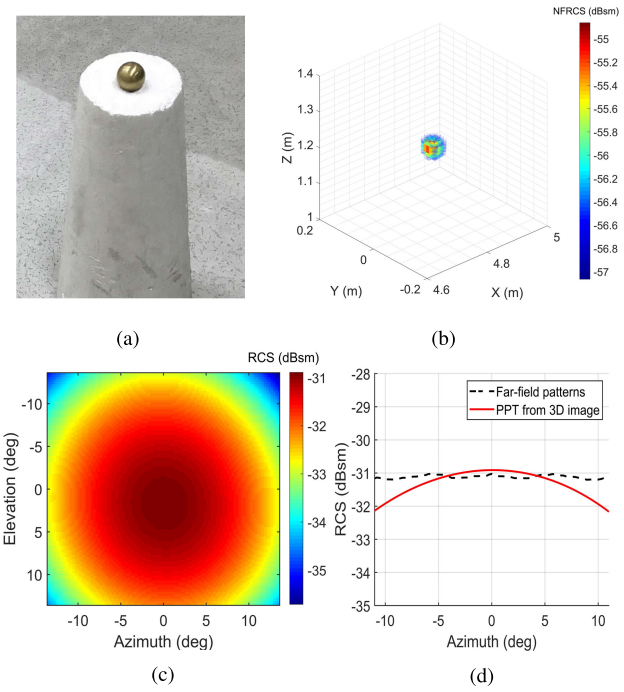

FIGURE 16. Measurement result of a metal sphere. (a) Target scene. (b) 3D NFRCS image.(c) Extrapolated RCS patterns from 3D image. (d) Profile result at $\theta = 0°$.

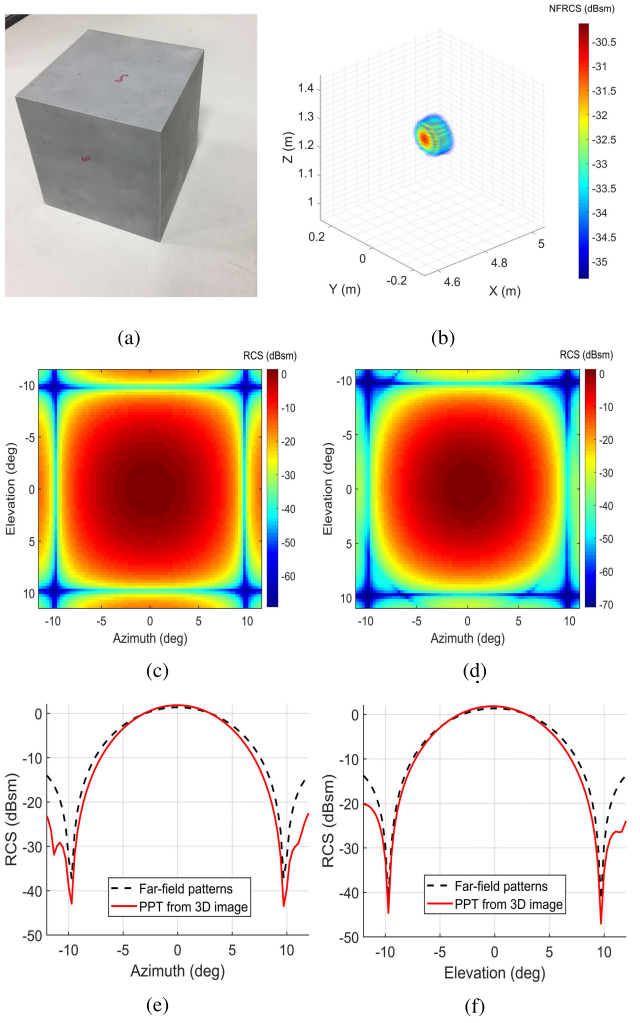

FIGURE 17. Measurement result of a metal cubic. (a) Target scene. (b) 3D NFRCS image.(c) Theoretical far-field RCS patterns. (d) Extrapolated RCS patterns from 3D image. (e) Profile result at $\theta = 0°$. (f) Profile result at $\varphi = 0°$.

center frequency and 2 GHz bandwidth. The targets include a -30 dBsm metal sphere (36 mm diameter) and a 0 dBsm metal cubic (100 mm length), as shown in Fig. 16(a) and Fig. 17(a).

Firstly, we use the proposed method to measure the metal sphere. Fig. 16(b) shows the 3D NFRCS image, and Fig. 16(c) shows the extrapolated RCS patterns from the 3D NFRCS image. Fig. 16(d) shows the profile result compared with theoretical value at $\theta = 0°$. Within $\pm 5°$ azimuth and elevation angles, the mean deviation is 0.15 dB. Within $\pm 10°$ azimuth and elevation angles, the mean deviation is 0.51 dB.

Then, we use the proposed method to measure the metal cubic. Fig. 17(b) shows the 3D NFRCS image. For comparison, Fig. 17(c) shows the theoretical far-field patterns via EM numerical simulation. Fig. 17(d) shows the extrapolated RCS patterns from the 3D NFRCS image. Fig. 17(e) shows the profile result compared with theoretical value at $\theta = 0°$. Fig. 17(f) shows the profile result compared with theoretical value at $\varphi = 0°$. Within $\pm 5°$ azimuth and elevation angles, the mean deviation is 0.61 dB. Within $\pm 10°$ azimuth and elevation angles, the mean deviation is 2.86 dB.

From these results, we can see that there is a high correlation between the PPT result and theoretical value, which verifies the validity of the proposed method in actual measurements.

VI. CONCLUSION

We present a 3D image-based RCS extrapolation method via the planar projective transforms (PPT).

Firstly, near-field 3D imaging SAR technique provides the 3D high resolution and extracts the complete reflectivity distribution of measured objects, which can ensure the proposed method has broad applicability to measuring point, surface, and complex scatterers. Secondly, the near-field patterns and far-field patterns are related to one another based on the integral transforms of reflectivity distribution, which ensures the proposed method can flexibly transform 3D NFRCS images into the multi-directional RCS patterns, including the azimuth and elevation directions. Thirdly, the proposed method adopts the image-based coherent accumulation, which observably enhances signal-to-noise and clutter ratio and relies less on equipment or physical means. Thus the proposed method can meet the requirements of broad applicability, high flexibility, and easy implementation.

Through the simulation results, the proposed method can provide the equivalent CATR result within $\pm 11°$ azimuth and elevation angles, and it is widely applicable to measuring the

point, surface, and complex scatterers. Through the experiment results, the proposed method has high accuracy for smooth objects, such as spheres. As for some objects with edges, such as cubic, there is some otherness because of edge effects. Our future work is to study the solution for edge effects and further improve the measurement accuracy.

REFERENCES

[1] E. F. Knott, "Radar cross section fundamentals," in *Radar Cross Section Measurements*, 2nd ed. Raleigh, NC, USA: SciTech, 2006, pp. 1–25.

[2] E. F. Knott, J. F. Shaeffer, and M. T. Tuley, "Physics and overview of electromagnetic scattering," in *Radar Cross Section*, 2nd ed. Raleigh, NC, USA: SciTech, 2004, pp. 63–110.

[3] D. W. Hess, "Introduction to RCS measurements," in *Proc. Loughborough Antennas Propag. Conf.*, Loughborough, U.K., Mar. 2008, pp. 37–44.

[4] L. Sevgi, Z. Rafiq, and I. Majid, "Radar cross section (RCS) measurements [Testing ourselves]," *IEEE Antennas Propag. Mag.*, vol. 55, no. 6, pp. 277–291, Dec. 2013. doi: 10.1109/MAP.2013.6781745.

[5] B. Svensson, R. Gustafsson, P. Hultman, P.-Å. Hansson, C. Augustsson, A. Jernberg, and C. Seupel, "A new compact antenna test range for EW-antenna system production testing," in *Proc. 11th Eur. Conf. Antennas Propag. (EUCAP)*, Paris, France, Mar. 2017, pp. 2585–2589.

[6] J. R. Descardeci and C. G. Parini, "Trireflector compact antenna test range," *IEE Proc.-Microw., Antennas Propag.*, vol. 144, no. 5, pp. 305–310, Oct. 1997.

[7] Y. Liu, X. Xu, and G. Xu, "MIMO radar calibration and imagery for near-field scattering diagnosis," *IEEE Trans. Aerosp. Electron. Syst.*, vol. 54, no. 1, pp. 442–452, Feb. 2018.

[8] J. Sun, L. Du, and W. Jiang, "Design of a 1-D sparse UWB MIMO array for near field RCS imaging system," in *Proc. Asia–Pacific Microw. Conf. (APMC)*, Nanjing, China, Dec. 2015, pp. 1–3.

[9] O. Tulgar and A. A. Ergin, "Improved pencil back-projection method with image segmentation for far-field/near-field SAR imaging and RCS extraction," *IEEE Trans. Antennas Propag.*, vol. 63, no. 6, pp. 2572–2584, Jun. 2015.

[10] K. L. Ford, J. C. Bennett, and D. G. Holtby, "Use of a plane-wave synthesis technique to obtain target RCS from near-field measurements, with selective feature extraction capability," *IEEE Trans. Antennas Propag.*, vol. 61, no. 4, pp. 2051–2057, Apr. 2013. doi: 10.1109/TAP.2012.2232636.

[11] N. Phruksahiran, S. Petchartee, and M. Chandra, "RCS measurements under GB-SAR environment," in *Proc. IEEE Conf. Antenna Meas. Appl. (CAMA)*, Chiang Mai, Thailand, Nov./Dec. 2015, pp. 1–3.

[12] W. Yue and Y. X. Beijing, "Performance analysis of radar high-resolution range profiling for stationary targets," in *Proc. IEEE Int. Conf. Signal Process., Commun. Comput. (ICSPCC)*, Xiamen, China, Oct. 2017, pp. 1–5.

[13] Y. Liu, H. Meng, G. Li, and X. Wang, "Velocity estimation and range shift compensation for high range resolution profiling in stepped-frequency radar," *IEEE Geosci. Remote Sens. Lett.*, vol. 7, no. 4, pp. 791–795, Oct. 2010.

[14] A. Broquetas, J. Palau, L. Jofre, and A. Cardama, "Spherical wave near-field imaging and radar cross-section measurement," *IEEE Trans. Antennas Propag.*, vol. 46, no. 5, pp. 730–735, May 1998.

[15] C. Hu, N. Li, W. Chen, and L. Zhang, "High-precision RCS measurement of aircraft's weak scattering source," *Chin. J. Aeronaut.*, vol. 29, no. 3, pp. 772–778, May 2016.

[16] J. W. Odendaal, L. Botha, and J. Joubert, "A full-scale static radar cross-section (RCS) measurement facility," *South African J. Sci.*, vol. 103, nos. 5–6, pp. 196–198, Jun. 2007.

[17] C. Larsson, "Nearfield RCS measurements of full scale targets using ISAR," in *Proc. 36th Antenna Meas. Techn. Assoc.*, Jan. 2014, pp. 79–84. [Online]. Available: http://portal.research.lu.se

[18] R. Bamler and P. Hartl, "Synthetic aperture radar interferometry," *Inverse Problems*, vol. 14, no. 4, pp. R1–R54, Aug. 1998.

[19] F. Gini, F. Lombardini, and M. Montanari, "Layover solution in multibaseline SAR interferometry," *IEEE Trans. Aerosp. Electron. Syst.*, vol. 38, no. 4, pp. 1344–1356, Oct. 2002.

[20] D. Sheen, D. McMakin, and T. Hall, "Near-field three-dimensional radar imaging techniques and applications," *Appl. Opt.*, vol. 49, no. 19, pp. E83–E93, 2010.

[21] Y. Wang and X. Li, "3-D imaging based on combination of the ISAR technique and a MIMO radar system," *IEEE Trans. Geosci. Remote Sens.*, vol. 56, no. 10, pp. 6033–6054, Oct. 2018. doi: 10.1109/TGRS.2018.2829912.

[22] Z. Li, J. Wang, J. Wu, and Q. H. Liu, "A fast radial scanned near-field 3-D SAR imaging system and the reconstruction method," *IEEE Trans. Geosci. Remote Sens.*, vol. 53, no. 3, pp. 1355–1363, Mar. 2015. doi: 10.1109/TGRS.2014.2338396.

[23] I. Gershenzon, Y. Brick, and A. Boag, "Shadow radiation iterative physical optics method for high-frequency scattering," *IEEE Trans. Antennas Propag.*, vol. 66, no. 2, pp. 871–883, Feb. 2018. doi: 10.1109/TAP.2017.2784439.

[24] M. Zhang, Y. Zhao, J.-X. Li, and P.-B. Wei, "Reliable approach for composite scattering calculation from ship over a sea surface based on FBAM and GO-PO models," *IEEE Trans. Antennas Propag.*, vol. 65, no. 2, pp. 775–784, Feb. 2017. doi: 10.1109/TAP.2016.2633066.

[25] J. Hu, J. Zhang, Q. Zhai, R. Zhan, and D. Lu, "ISAR imaging using a new stepped-frequency signal format," *IEEE Trans. Geosci. Remote Sens.*, vol. 52, no. 7, pp. 4291–4305, Jul. 2014.

[26] S. R. J. Axelsson, "Beam characteristics of three-dimensional SAR in curved or random paths," *IEEE Trans. Geosci. Remote Sens.*, vol. 42, no. 10, pp. 2324–2334, Oct. 2004. doi: 10.1109/TGRS.2004.834802.

[27] S. Jun, Z. Xiaoling, Y. Jianyu, and W. Chen, "APC trajectory design for 'one-active' linear-array three-dimensional imaging SAR," *IEEE Trans. Geosci. Remote Sens.*, vol. 48, no. 3, pp. 1470–1486, Mar. 2010. doi: 10.1109/TGRS.2009.2031430.

[28] S. Wei, X. Zhang, and J. Shi, "Spaceborne-airborne bistatic linear array SAR high resolution 3-D imaging based on sparsity exploiting," in *Proc. 19th Int. Conf. Inf. Fusion (FUSION)*, Heidelberg, Germany, Jul. 2016, pp. 1518–1522.

[29] I. J. LaHaie, "Overview of an image-based technique for predicting far-field radar cross section from near-field measurements," *IEEE Antennas Propag. Mag.*, vol. 45, no. 6, pp. 159–169, Dec. 2003. doi: 10.1109/MAP.2003.1282192.

[30] S. Jun, Z. Xiaoling, S. Han, and Y. Jianyu, "Explanation of synthetic aperture 3-D imaging technique via EFIE," in *Proc. 3rd Int. Asia–Pacific Conf. Synth. Aperture Radar (APSAR)*, Seoul, South Korea, Sep. 2011, pp. 1–4.

[31] D. G. Falconer, "Extrapolation of near-field RCS measurements to the far zone," *IEEE Trans. Antennas Propag.*, vol. AP-36, no. 6, pp. 822–829, Jun. 1988.

LING PU received the B.S. degree in electronic engineering from the University of Electronic Science and Technology of China, Chengdu, China, in 2014, where he is currently pursuing the Ph.D. degree in signal and information processing.

His research interests include radar signal processing, SAR systems, and RCS measurements.

XIAOLING ZHANG received the B.S., M.Sc., and Ph.D. degrees in electronic engineering from the University of Electronic Science and Technology of China (UESTC), Chengdu, China, in 1985, 1988, and 2000, respectively, where she is currently a Professor.

In 2000, she joined UESTC. Her research interests include radar signal processing and classification/recognition.

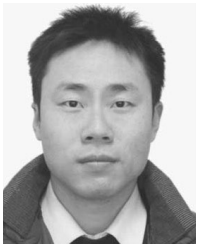

JUN SHI received the B.S., M.Sc., and Ph.D. degrees in electronic engineering from the University of Electronic Science and Technology of China (UESTC), Chengdu, China, in 2002, 2005, and 2009, respectively, where he is currently an Associate Professor.

In 2009, he joined UESTC. His research interests include radar signal processing and SAR systems.

SHUNJUN WEI received the B.S., M.Sc., and Ph.D. degrees in electronic engineering from the University of Electronic Science and Technology of China (UESTC), Chengdu, China, in 2006, 2009, and 2013, respectively, where he is currently an Associate Professor.

In 2014, he joined UESTC. His research interests include radar signal processing and SAR systems.

LIANG LI received the B.S. degree from the School of Computer and Communication Engineering, Northeastern University at Qinhuangdao, Qinhuangdao, China, in 2016, where he is currently pursuing the Ph.D. degree in signal and information processing.

XINXIN TANG received the B.S. degree in electronic engineering from the Southwest University of Science and Technology, Mianyang, China, in 2012. She is currently pursuing the Ph.D. degree in signal and information processing with University of Electronic Science and Technology of China (UESTC), where she joined in 2013.

Her research interests include radar signal processing and classification/recognition.